In vivo evaluation of demyelination and remyelination in a nerve crush injury model

E. Bélanger,[1,2] **F. P. Henry,**[3] **R. Vallée,**[1,2] **M. A. Randolph,**[3]
I. E. Kochevar,[3] **J. M. Winograd,**[3] **C. P. Lin,**[3] **and D. Côté**[1,2]

[1]*Centre de Recherche Université Laval Robert-Giffard (CRULRG), Université Laval,*
Québec, Qc, G1J 2G3, Canada
[2]*Centre d'Optique, Photonique et Laser (COPL), Université Laval,*
Québec, Qc, G1V 0A6, Canada
[3]*Massachusetts General Hospital (MGH), Harvard Medical School,*
50 Blossom Street, Boston, Massachusetts 02114, USA

*daniel.cote@crulrg.ulaval.ca

Abstract: Nerves of the peripheral nervous system have, to some extent, the ability to regenerate after injury, particularly in instances of crush or contusion injuries. After a controlled crush injury of the rat sciatic nerve, demyelination and remyelination are followed with functional assessments and imaged both *ex vivo* and *in vivo* over the course of 4 weeks with video-rate coherent anti-Stokes Raman scattering (CARS) microscopy. A new procedure compatible with live animal imaging is developed for performing histomorphometry of myelinated axons. This allows quantification of demyelination proximal and remyelination distal to the crush site *ex vivo* and *in vivo* respectively.

References and links

1. M. D. Duncan, J. Reintjes, and T. J. Manuccia, "Scanning coherent anti-Stokes Raman microscope," Opt. Lett. **7**, 350–352 (1982).
2. A. Zumbusch, G. R. Holtom, and X. S. Xie, "Three-dimensional vibrational imaging by coherent anti-Stokes Raman scattering," Phys. Rev. Lett. **82**, 4142–4145 (1999).
3. C. L. Evans, E. O. Potma, M. Puoris'haag, D. Côté, C. P. Lin, and X. S. Xie, "Chemical imaging of tissue in vivo with video-rate coherent anti-Stokes Raman scattering microscopy," Proc. Natl. Acad. Sci. U.S.A. **102**, 16807–16812 (2005).
4. T. B. Huff and J.-X. Cheng, "In vivo coherent anti-Stokes Raman scattering imaging of sciatic nerve tissue," J. Microsc. **225**(2), 175–82 (2007).
5. F. P. Henry, D. Côté, M. A. Randolph, E. A. Z. Rust, R. W. Redmond, I. E. Kochevar, C. P. Lin, and J. M. Winograd, "Real-time in vivo assessment of the nerve microenvironment with coherent anti-Stokes Raman scattering microscopy," Plast. Reconstr. Surg. **123(2S)**, 123S–130S (2009).
6. H. Wang, Y. Fu, P. Zickmund, R. Shi, and J.-X. Cheng, "Coherent anti-stokes Raman scattering imaging of axonal myelin in live spinal tissues," Biophys. J. **89**, 581–591 (2005).
7. E. Bélanger, S. Bégin, S. Laffray, Y. De Koninck, R. Vallée, and D. Côté, "Quantitative myelin imaging with coherent anti-Stokes Raman scattering microscopy: alleviating the excitation polarization dependence with circularly polarized laser beams," Opt. Express **17**(21), 18419–18432 (2009).
8. J. Imitola, D. Côté, S. Rasmussen, X. S. Xie, Y. Liu, T. Chitnis, R. L. Sidman, C. P. Lin, and S. J. Khoury, "Multimodal coherent anti-Stokes Raman scattering microscopy reveals microglia-associated myelin and axonal dysfunction in multiple sclerosis-like lesions in mice," J. Biomed. Opt. **16**(2), 021,109 (2011).

9. C. Evans and X. S. Xie, "Coherent anti-Stokes Raman scattering microscopy: chemical imaging for biology and medicine," Annu. Rev. Anal. Chem. **1**, 883–909 (2008).

10. S. Bégin, E. Bélanger, S. Laffray, R. Vallée, and D. Côté, "In vivo optical monitoring of tissue pathologies and diseases with vibrational contrast," J. Biophoton. **2**(11), 632–642 (2009).

11. T. T. Le, S. Yue, and J.-X. Cheng, "Shedding new light on lipid biology with coherent anti-Stokes Raman scattering microscopy," J. Lipid. Res. **51**(11), 3091–3102 (2010).

12. J. P. Pezacki, J. A. Blake, D. C. Danielson, D. C. Kennedy, R. K. Lyn, and R. Singaravelu, "Chemical contrast for imaging living systems: molecular vibrations drive CARS microscopy," Nat. Chem. Biol. **7**(3), 137–145 (2011).

13. J. R. Bain, S. E. Mackinnon, and D. A. Hunter, "Functional evaluation of complete sciatic, peroneal, and posterior tibial nerve lesions in the rat," Plast. Reconstr. Surg. **83**(1), 129–138 (1989).

14. I. Veilleux, J. A. Spencer, D. P. Biss, D. Côté, and C. P. Lin, "In vivo cell tracking with video rate multimodality laser scanning microscopy," IEEE J. Sel. Top. Quantum Electron. **14**, 10–18 (2008).

15. J. S. O'Brien and E. L. Sampson, "Lipid composition of the normal human brain: gray matter, white matter, and myelin," J. Lipid. Res. **6**(4), 537–544 (1965).

16. M. Guizar-Sicairos, S. T. Thurman, and J. R. Fienup, "Efficient subpixel image registration algorithms," Opt. Lett. **33**(2), 156–158 (2008).

17. W. Niblack, *An Introduction to Digital Image Processing* (Prentice-Hall International, 1986).

18. G. Veshapidze, M. L. Trachy, M. H. Shah, and B. D. DePaola, "Reducing the uncertainty in laser beam size measurement with a scanning edge method," Appl. Opt. **45**(32), 8197–8199 (2006).

19. M. Coleman, "Axon degeneration mechanisms: commonality amid diversity," Nat. Rev. Neurosci. **6**(11), 889–898 (2005).

20. K. Hirata and M. Kawabuchi, "Myelin phagocytosis by macrophages and nonmacrophages during Wallerian degeneration," Microsc. Res. Tech. **57**(6), 541–547 (2002).

21. J. Knöferle, J. C. Koch, T. Ostendorf, U. Michel, V. Planchamp, P. Vutova, L. Tönges, C. Stadelmann, W. Brück, M. Bähr, and P. Lingor, "Mechanisms of acute axonal degeneration in the optic nerve in vivo," Proc. Natl. Acad. Sci. U.S.A. **107**(13), 6064–6069 (2010).

22. R. Haralick, K. Shanmuga, and I. Dinstein, "Textural Features For Image Classification," IEEE Trans. Syst. Man Cyb. **SMC3**(6), 610–621 (1973).

23. M. Balu, G. Liu, Z. Chen, B. J. Tromberg, and E. O. Potma, "Fiber delivered probe for efficient CARS imaging of tissues," Opt. Express **18**(3), 2380–2388 (2010).

24. S. Murugkar, B. Smith, P. Srivastava, A. Moica, M. Naji, C. Brideau, P. K. Stys, and H. Anis, "Miniaturized multimodal CARS microscope based on MEMS scanning and a single laser source," Opt. Express **18**(23), 23796–23804 (2010).

1. Introduction

Peripheral nerve pathology, whether through direct injury (trauma) or chronic disease (carpal tunnel compressive neuropathy) results in a disability that has widespread repercussions for both personal and occupational rehabilitation. While complete division of a nerve can be directly observed and managed appropriately with standard microsurgery, the spectrum of injury related to crushed nerves or chronic neuropathies cannot be accurately assessed. The ability to observe the microarchitecture of the nerve, in particular its level of myelination, is limited at present to destructive histological techniques that are not appropriate in a clinical setting and therefore currently there is no method that can help a clinician assess nerve health *in vivo* following injury. Electrical studies, although a useful diagnostic technique, cannot in the early phase of injury distinguish between nerves with minor or severe internal disruption. Furthermore, only after recovery has occurred over a period of several months can such a determination be made empirically. This "wait and see" approach prolongs the period of muscle denervation distally, lengthens the time to ultimate recovery if surgical reconstruction is required, and ultimately hastens the time after which meaningful reconstruction, particularly of motor neuron lesions, is no longer possible. A technique which would provide information to allow for grading of the nerve injury would be a valuable clinical tool in terms of both a diagnostic and prognostic indication of functional recovery.

Following neural injury, axonal demyelination coupled with subsequent remyelination over time may be used as an indicator of both severity of injury and degree of neural recovery expected. The degree of axonal remyelination observed following initial insult corresponds di-

rectly to the level of functional recovery achieved. Current methods of assessing axonal myelination rely on destructive histological techniques (*ex vivo*, transverse slice, mechanically cut) which are not suitable in the clinical setting. More recently a novel imaging modality based on CARS [1, 2] has been demonstrated to be sensitive to lipid-rich cells such as adipocytes [3], Schwann cells [4, 5] and oligodendrocytes [6–8] without the use of exogenous labeling. This technique utilizes the CH_2 symmetric stretch vibration that is present in lipids by exciting it with two lasers tuned to different wavelengths such that their frequency difference corresponds to the frequency of the vibration. Through a vibrationally resonant third-order nonlinear process, a photon at a higher frequency is emitted to provide lipid-based contrast. By virtue of being a nonlinear process, it benefits from three-dimensional sectioning and high spatial resolution similar to two-photon excitation fluorescence [9–12]. When combined with distortion-free images (without breathing and heartbeat artifacts) obtained with *in vivo* video-rate microscopy, CARS imaging is ideally positioned to quantify peripheral nerve myelination in live animals over an extended period of time. This longitudinal assessment of neural injury provides unique histology without compromising the nerve itself, i.e. in its native state. Standard histology is usually done *ex vivo* on transverse sections of fixed nerve slices, a preparation not suitable for *in vivo* evaluation due to its intrinsic destructive nature. Reconstruction of transverse sections from *z*-stacks can provide similar information when CARS contrast is used [7]. Yet, even with video-rate imaging, it is challenging to obtain three-dimensional data that allows for high quality *z*-stack reconstruction. For this reason, we propose a new procedure compatible with live animal imaging. Histomorphometry based on CARS images is extracted from frames recorded from the coronal plane of the sciatic nerve.

In this paper, the rat sciatic nerve is used as a model of Wallerian degeneration in which we perform myelin histomorphometry on images obtained with CARS tuned to lipid-based contrast. After a controlled crush injury, the nerves are surgically exposed and imaged *in vivo* and *ex vivo* in the coronal plane with confocal reflectance and CARS microscopy at different time points and at different locations on the sciatic nerve. We quantify demyelination proximal and remyelination distal to the crush site *ex vivo* and *in vivo* respectively. From this we show that CARS microscopy may be use as a reliable, non-destructive, *in vivo* technique with sufficient accuracy to assess axonal myelination of normal and injured peripheral nerves.

2. Materials and methods

2.1. Animal model

We have used the sciatic nerve of Sprague Dawley rats as a model for this study. Approval was obtained from our local institutional animal care and use committee. Surgical exposure of the sciatic nerve was achieved by means of a dorsolateral muscle splitting incision. A standardized demyelinating crush injury was reproduced in all animals (14) by means of a #5 jeweler's forceps held closed across the nerve for 30 seconds. Functional assessment of the sciatic nerve was carried out by means of a walking track analysis. Following sciatic nerve injury and during subsequent recovery, the hindprint of the rat undergoes several morphological changes from which a sciatic function index (SFI) can be calculated [13]. Prints were obtained by coating the animal hindpaws in ink and allowing it to walk down a paper-lined track. The resulting SFI allows for a longitudinal functional assessment of sciatic nerve regeneration. For the purpose of imaging, the animal was anaesthetized (intraperitoneal injection of pentobarbital) and surgery was performed to expose the sciatic nerve. The animal is then mounted on an adapted stage that is incorporated into a custom-built upright multimodal video-rate microscope. Imaging with confocal reflectance (detecting the pump beam) and CARS is performed simultaneously.

2.2. CARS microscope

The custom-made video-rate laser scanning microscope and laser sources were described previously [3, 14]. Briefly, the CARS microscope consists of two synchronized laser sources with a custom-built microscope. The Stokes pulse is provided by a 10 W, 7 ps Nd:Vanadate pulsed laser (picoTRAIN, High Q Laser) operating at 1064 nm while the pump pulse, at a wavelength of 816.8 nm, is obtained from a synchronously pumped OPO (Levante Emerald ps, APE) generating approximately 400 mW at 80 MHz. Both beams are recombined spatially and temporally with a dichroic mirror mounted on a delay line and are sent to the video-rate laser scanning microscope acquiring two channels simultaneously at a frame rate of 30 images per second. The confocal reflectance channel is captured by an avalanche photodiode (InGaAs, CMC Electronics) while the CARS channel is recorded with a red-sensitive photomultiplier tube (R3896, Hamamatsu) in a non-descanned configuration. After accounting for losses through the scanning system, the dichroics and the $63\times$ objective (UIS-UPLAPO, 1.2 NA / w, Olympus), a total of 50 to 100 mW (pump and Stokes beams) was incident on the sample. The contrast obtained with CARS microscopy arises because the frequency difference of the pump and Stokes beam is chosen to resonantly excite the CH_2 symmetric stretch vibrational mode at 2845 cm^{-1}, predominantly localized in lipids. Schwann cells and the myelin they produce are lipid-rich molecules [15] and account for the majority of the CARS signal in this case.

2.3. Image acquisition

Confocal reflectance is used as a guidance modality to confirm position and nature of the tissue in question prior to imaging with CARS. During the imaging session, animal breathing leads to lateral shifts between subsequent frames. A real-time movement correction algorithm, based on tracking the maximum of the 2d cross-correlation function [16] of following frames, is used to permit long integration times. Axial movement of the animal (up / down) is reduced by mechanically restricting leg movements. An image is referred to a frame recorded in the coronal plane (inset of Fig. 1(b)) of the sciatic nerve as opposed to a transverse image (inset of Fig. 1(a)) which is rendered from a z-stack of multiple images recorded in the coronal plane. When axial movement is minimized, z-stacks (60 images, 1 μm apart) are acquired to reconstruct transverse images corresponding to the standard histology paradigm. After the imaging session, the animal is sacrificed to permit *ex vivo* CARS imaging.

2.4. Image processing for histology in the transverse plane

Image analysis was performed with an in-house software [7] implemented in Matlab (Mathworks, Natick, Massachusetts, USA) and with ImageJ (NIH, Bethesda, Maryland, USA). To assess the myelin health, z-stacks of images were acquired and transverse views were rendered with the freely accessible Volume Viewer plugin. Then, region of interests (ROIs) that include a myelinated axon were manually cropped from the whole dataset of transverse images. All ROIs were resampled by a factor of 4 with a bicubic algorithm. Each individual axon was thresholded with an automatic adaptive Niblack algorithm [17], to avoid any user bias. Local window size was set to 21 pixels and weight of the standard deviation contribution to 0.55 (i.e. the k-value). The threshold parameters were set empirically on a subset of images of a control animal and kept constant for all subsequent measurements. At that time, an automated function determined the inner and outer boundaries of the circular myelin sheath on the binary image, from which the diameter of the axon and that of the fiber are mathematically computed based on the area of their respective regions. Finally, the g-ratio (ratio of the axon to the fiber diameter) is calculated by dividing the two previous measurements.
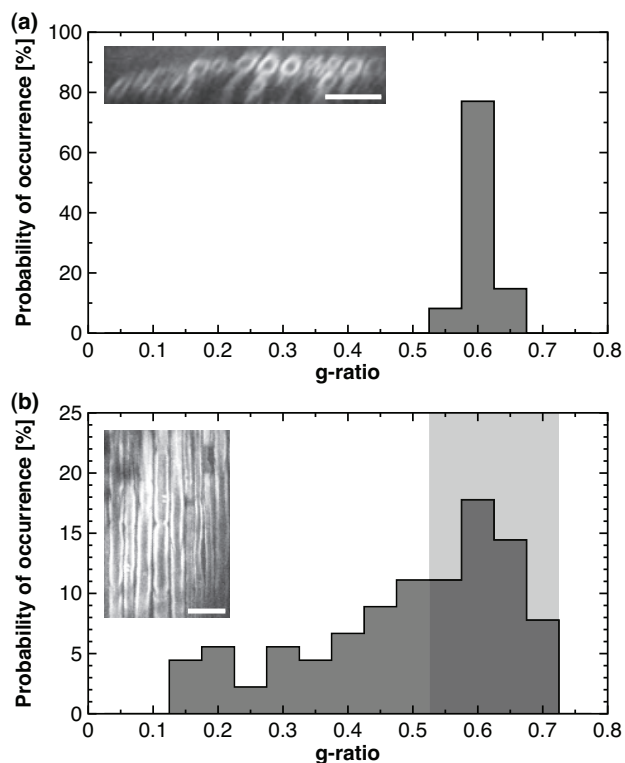
Fig. 1. CARS histomorphometry in transverse and coronal planes. Probability histogram of g-ratio measurements extracted from (a) reconstructed transverse planes and from (b) the *z*-stack of coronal planes. (a, inset) Typical CARS image in the transverse plane. (b, inset) Typical CARS image in the coronal plane. All scale bars are 25 μm.

2.5. *Image processing for histology in the coronal plane*

Image analysis was performed with Matlab and ImageJ. Morphology based on CARS images was extracted from frames recorded from the coronal plane of the sciatic nerve. The proposed approach is an analogy of the laser beam size measurement method making use of a scanning edge [18]. First, individual myelinated axons were manually cropped from the original dataset. Great care is taken to make sure that rectangular ROIs were parallel to their respective axon. Then, all ROIs were resampled by a factor of 4 with a bicubic algorithm. At this time, all the individual line profiles coming from a particular ROI were averaged to obtain a single representative line profile of the fiber. At this point, a linear baseline subtraction was performed in order to level the representative line profile on a straight line. The leveled representative line profile was then normalized by dividing every of his points by its maximum value. A cumulative integral was numerically computed on the resulting line profile. The fiber and axon diameter are determined by the position of the edges of the fiber and axon diameters. The edges position correspond to a width of half of the contributed area of each peak of the line profile to the cumulative integral (i.e. roughly 12.5 %, 37.5 %, 62.5 % and 87.5 %). The limits were set empirically on a subset of images of a control animal and kept constant for all subsequent measurements. Figure 2(c) shows a typical leveled line profile (solid line) overlaid with its cumulative integral (dashed line). The dotted lines highlight the positions that were automatically determined by the cumulative integral to be the edges of the fiber and axon diameters. The g-ratio was calculated
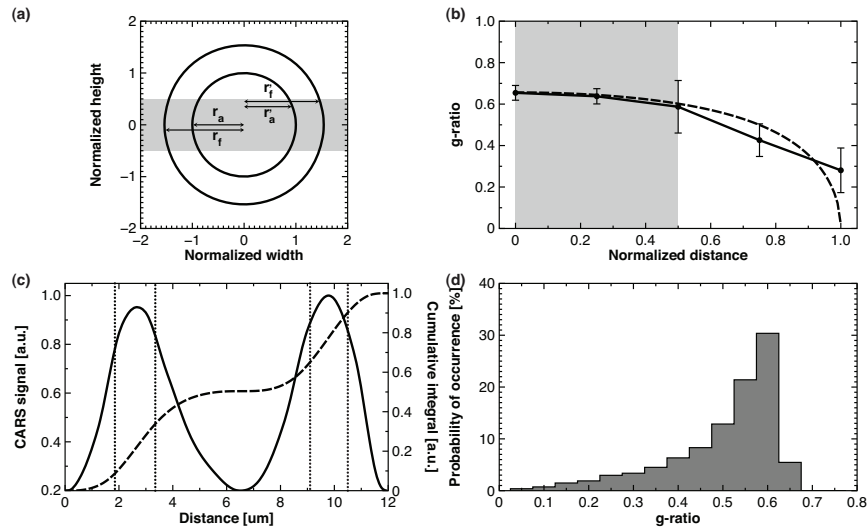
Fig. 2. (a) Scheme of the imaging plane relative the fiber and axon location (r_a: axon radius, r_f: fiber radius, r'_a: biased axon radius and r'_f: biased fiber radius). (b) Measured g-ratio versus the normalized displacement from the center of the axon (solid: experimental and dashed: simulated). (c) Leveled line profile (solid) overlaid with its cumulative integral (dashed) and the edges of the fiber and axon diameter (dotted). (d) Theoretical biased probability histogram of g-ratio measurements.

by dividing the axon by the fiber diameter. Myelin thickness was computed by a subtracting the axon to the fiber diameter and then dividing by the factor 2.

2.6. Statistical analysis

Values are expressed in terms of means ± standard error of the mean (SEM) unless otherwise stated. Statistical analysis of the data was performed using Matlab. Values of $p \leq 0.05$ were considered statistically significant (*), $p \leq 0.01$ were considered highly statistically significant (**) and $p \leq 0.001$ were considered extremely statistically significant (***). Mann-Whitney U-test was used to evaluate the differences in medians of g-ratio distributions and myelin thickness prevalence at various position along a crushed nerve (Fig. 4(d)) and at different time points post-crush (Fig. 6(b)) respectively.

3. Results

3.1. Myelin histomorphometry in the transverse and coronal plane of CARS images

The objective of this section is to demonstrate that it is possible to provide accurate estimates of myelin histomorphometric parameters from CARS images of live uncut tissue, the two most important parameters being the g-ratio and the myelin thickness. With this method, preparation and cutting artifacts inherent to standard histology are avoided. Histomorphometric analysis can be performed on transverse images obtained by three-dimensional reconstruction of a *z*-stack (Fig. 1(a)), or on coronal images (Fig. 1(b)). The g-ratio histogram extracted from transverse images of sciatic nerves of Fig. 1(a) is obtained from 61 morphometric measurements (1 animal, 70 transverse images) and reveals a mean g-ratio of 0.60 with a standard deviation of 0.02. The g-ratio histogram for the same nerve section, but instead analyzed on coronal slices, is shown on Fig. 1(b). The g-ratio histogram shows 90 measurements (1 animal, 60 images) and

illustrates that under a random sampling of the position of the imaging plane throughout the axon diameter, the distribution is skewed towards smaller values. We hypothesize that the upper half of the g-ratio distribution, i.e. every measurement over the median, is minimally affected and is suitable for histomorphometry (region highlighted in light gray on Fig. 1(b)). In the present case, the mean g-ratio of every measurement over the 50th percentile is 0.62 ± 0.04.

As is shown on Fig. 2(a) and Fig. 2(b), the randomly positioned imaging plane leads to measured g-ratio within 15% of the nominal g-ratio value 50% of the time. Importantly, the value is always underestimated and never overestimated. A simple model illustrated on Fig. 2(a) reveals the trend in g-ratio bias on Fig. 2(b) (dashed line: calculation, solid line: experimental data points from Fig. 1(b)). The normalized displacement is defined as the distance from the axon center divided by its diameter. Myelin parameters on coronal images are extracted with the procedure described in section 2.5 (see Fig. 2(c)). The predicted asymmetrical resulting histogram, for a fiber distribution similar to Fig. 1(a), is shown on Fig. 2(d) and confirms that every measurement over the 50th percentile is minimally affected. Therefore, with a random sampling of imaging plane positions and a large number of measurements, this technique is satisfactory for studying neuropathies in which a single population of hypomyelinated axons is expected.

3.2. Myelin histomorphometry reveals demyelination on ex vivo crushed sciatic nerve

Figure 3 shows a large-scale and high-resolution CARS map of an *ex vivo* crushed sciatic nerve at the millimeter scale at 1 week post-injury. This mosaic is a collection of images (i.e. tiles) manually stitched together. Each individual tile measures 435 μm $\times$ 435 μm. This map measures approximately 0.5 mm width by 4 mm long. The vertical scale indicates the approximate transition from the healthy to the proximal and from the proximal to the distal part of the lesion. Well aligned and globally organized myelin sheaths are clearly observed in the healthy region. In the proximal region, myelin swelling and spheroids appear. The distal region is mostly filled with myelin debris with no distinguishable sign of myelinated axons.

Figure 4(a)–4(c) shows typical snapshots (corresponding to the 3 ROIs of Fig. 3), of the healthy, proximal and distal region of the lesion at 1 week post-crush respectively. The g-ratio histogram is measured at different locations along the crushed nerve and its asymmetrical distribution is used to extract the minimally biased g-ratios. The mean g-ratio increases from approximately 0.58-0.60 (1 animal, 6 images, 19, 21 and 23 measurements) in the healthy region to 0.63-0.65 (1 animal, 12 images, 25, 23, 20 and 13 measurements) proximal to the lesion site, as shown in Fig. 4(d). All mean g-ratios in the proximal zone were compared (Mann-Whitney U-test) with the central point of the healthy region (indicated by a light gray square). This analysis reveals a highly statistically significant (**) to extremely statistically significant increases (***) between the different locations along the crushed nerve suggesting that healthy and proximal regions have different axonal myelination.

3.3. Myelin histomorphometry reveals remyelination on in vivo crushed sciatic nerve

Following a crushed nerve injury, axonal damage and demyelination are expected to occur mostly distal to the point of injury. The nerve also demyelinates to the proximal node of Ranvier [19]. The superficial layers of the sciatic nerves were imaged at different time points of recovery after injury, as shown in Fig. 5. The control image (Fig. 5(d)) shows myelin sheaths with normal myelin thickness, as expected from healthy nerves. Figure 5(a), Fig. 5(b) and Fig. 5(c) show myelin sheaths proximal to the crush site at 2, 3 and 4 weeks post-injury respectively. Only modest changes are observed to the myelinated axons architecture, as expected for the proximal part of the lesion. In fact, minor myelin swelling is observed with diminished effect over time. However, the situation is very different distal to the lesion site. Figure 5(e)
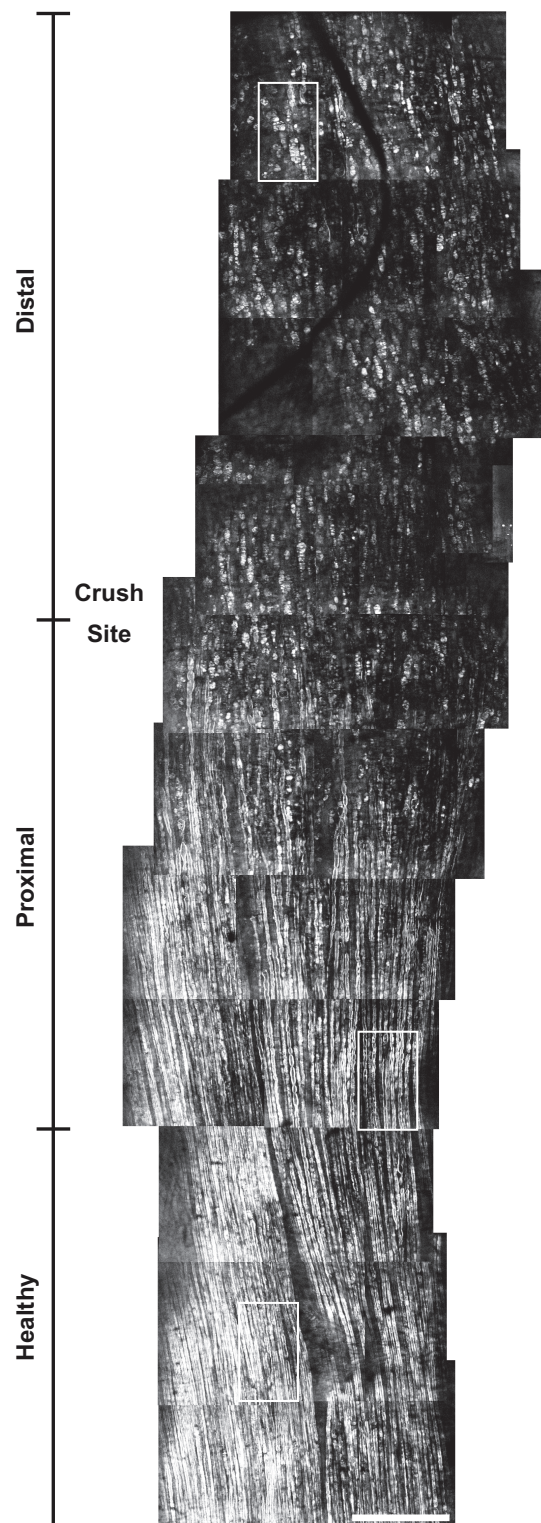
Fig. 3. Large-scale and high-resolution CARS map of a crushed sciatic nerve at the millimeter scale at 1 week post-injury. Three ROIs depicting healthy, proximal and distal regions of the nerve are highlighted. Scale bar is 250 μm.
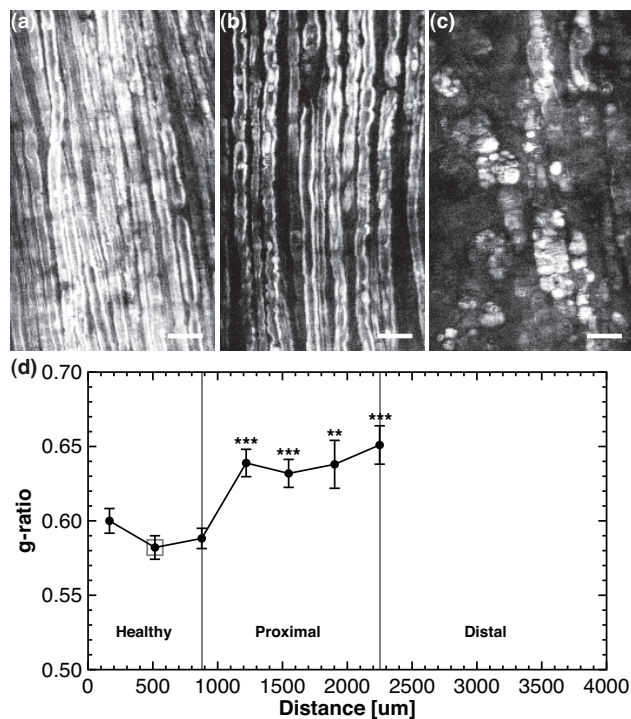
Fig. 4. Histomorphometry on *ex vivo* crushed sciatic nerve 1 week post-injury. (a)-(c) Snapshots of the healthy, proximal and distal region of the lesion respectively, corresponding to the 3 ROIs of Fig. 3. (d) The g-ratio versus the position along the crushed sciatic nerve. All scale bars are 25 μm.
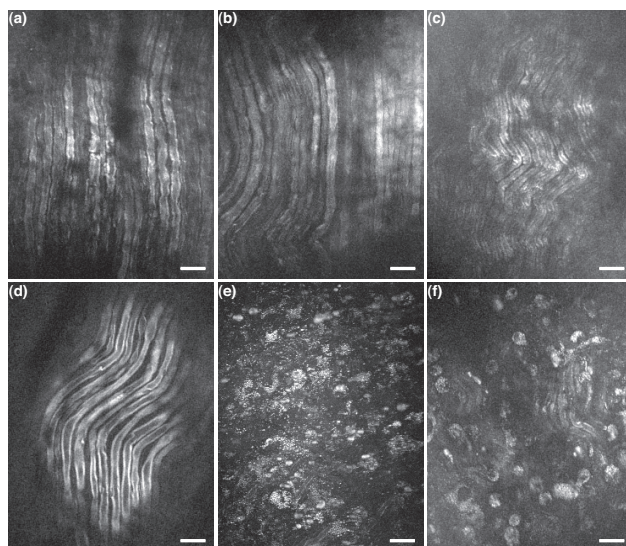

Fig. 5. *In vivo* CARS images of crushed sciatic nerves at different time points of recovery. (a-c) Myelin sheaths proximal to the crush site at 2, 3 and 4 weeks post-injury respectively. (d) Myelin sheaths of a control sciatic nerve. (e) and (f) Myelin sheaths distal to the crush site at 2 and 4 weeks post-crush respectively. All scale bars are 25 μm.

and Fig. 5(f) reveal a large amount of myelin debris with very few myelinated axons at 2 and 4 weeks post-crush respectively. Myelin debris are organized in a cell-like shapes suggesting that they are phagocytosed by either Schwann cells or macrophages [20].

Loss of function following injury is seen to partially recover over the course of 4 weeks. While the timeframe for remyelination can vary between animals and injuries it is expected to begin roughly 1 week following neural insult and upon cessation of the initial inflammatory response [19]. This slow process is mirrored by the return of motor function as demonstrated in Fig. 6(a) by a constant increase of the SFI starting at 1 week post-crush (14 animals). In order
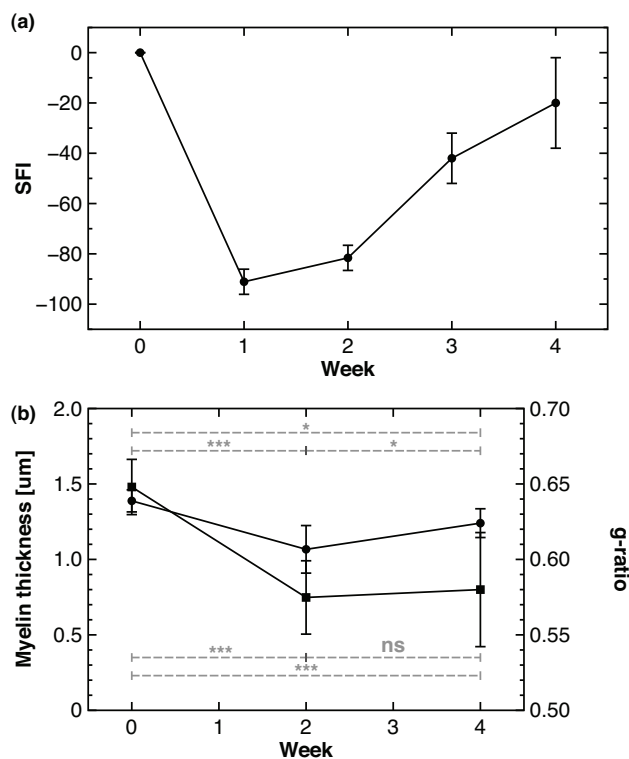

Fig. 6. Behavioural assessment and histomorphometry on *in vivo* CARS images of crushed sciatic nerves distal to the lesion at different time points. (a) SFI and (b) myelin thickness (circles) and the g-ratio (squares) versus time.

to address remyelination *in vivo* at the cellular level, as opposed to behavioural assessment, the myelin thickness (circles) and the g-ratio (squares) have been measured distal to the lesion at 2 and 4 weeks post-injury and is illustrated in Fig. 6(a) and Fig. 6(b) respectively. The myelin thickness decreases from 1.4 to 1.1 μm (***) from the control (7 animals, 412 images, 233 measures) to 2 weeks post-crush (1 animal, 94 images, 15 measures), unravelling a significant demyelination. At 4 weeks (1 animal, 100 images, 6 measures), myelin thickness augments up to 1.2 μm (*), showing a partial remyelination. However, the level of myelination is still lower than in the control (*).

4. Discussion

The gold standard for myelin histomorphometry is to compute morphological parameters on transverse images on ultra-thin slices of fixed tissue. With myelin CARS imaging, it is possible

to use this approach *in vivo* with optical sectioning and reconstructed *z*-stacks to obtain reliable metrics as shown in Fig. 1(a) and in [7]. However, this paradigm is often difficult in live animal due to animal movement (breathing and heartbeat): *z*-stack recording requires a stable tissue volume to avoid any distortion for the duration of the acquisition which can be several seconds. On the other hand, a single image at video-rate can easily be acquired distortion-free. Histomorphometry in the coronal plane is fully compatible with live animal imaging since it requires solely a collection of single images randomly positioned inside the axon diameter rather than a well registered *z*-stack. This results in a g-ratio distribution that is often underestimated; a single bias-free g-ratio can be calculated with transverse plane images (Fig. 1(a)), whereas on coronal images, a positively skewed distribution of g-ratios is obtained (as shown on Fig. 1(b) and Fig. 2(d)).

We applied this method *in vivo* for studying sciatic nerve crush injuries. Figure 4(d) shows an increase of the g-ratio (i.e. a thinning of myelin) in the proximal region of the lesion 1 week post-injury. Similar findings have also been reported recently in an *in vivo* model of acute axonal degeneration in the optic nerve [21]. Figure 6(b) shows a decrease of the myelin thickness and of the g-ratio simultaneously distal to the lesion over time. This behaviour has also been pointed out by [21] and explained it by axons possessing a condensed axoplasm.

Images post-crush (especially at 2 weeks) are difficult to acquire because of the large inflammation in the vicinity of the lesion. A thickening of the epinerium as well as an increased vascularization surrounding the lesion site limit the penetration depth, both by lowering excitation and detection of the back-scattered photons. This results in a limited amount of measures in the pathological states compared to the control, limiting generalization of our results. However, demyelination arising from chronic compression injuries do not result in dramatic inflammatory responses and in these cases, CARS microscopy would be very appropriate.

The g-ratio and the myelin thickness were not totally adequate to describe the axons morphology. For example, the whole distal part of the large-scale and high-resolution CARS map in Fig. 3 cannot be quantified with these standards metrics. Also, only a few myelinated axons have been found in Fig. 5(c) and Fig. 5(f) suggesting that the use of new metrics such as textures analysis [22] could complement the usual morphological parameters in depicting the complete structural changes arising from demyelinating pathologies.

With the rapid emergence of hand-held probes [23] and microendoscopes [24], CARS microscopy has the potential to become an experimental and clinical tool in the field of peripheral nerve pathologies. It would provide nondestructive, real-time and label-free information to allow for both diagnostic and prognostic at cellular level.

5. Conclusion

In conclusion, video-rate CARS microscopy was used to image the microenvironment of the sciatic nerve *ex vivo* and *in vivo*. Histomorphometry in the coronal plane, an approach compatible with live animal imaging, has been used to assess axonal myelination. Demyelination and subsequent remyelination have been observed, quantified, and correlated with behavioural assessment. This nondestructive, real-time, *in vivo* microscopy may be useful in the near future as an experimental and clinical tool in the field of peripheral nerve pathologies.

Acknowledgments